High and flat spectral responsivity of quartz tuning fork used as infrared photodetector in tunable diode laser spectroscopy (F) (SCI)

(iD) **Tingting Wei,** (iD) **Andrea Zifarelli,** (iD) **Stefano Dello Russo, et al.**

COLLECTIONS

(F)   This paper was selected as Featured

(SCI)   This paper was selected as Scilight

openaccess

View Online   Export Citation   CrossMark

High and flat spectral responsivity of quartz tuning fork used as infrared photodetector in tunable diode laser spectroscopy

Tingting Wei,[1,2] Andrea Zifarelli,[1,3] Stefano Dello Russo,[1,3] Hongpeng Wu,[1,2] Giansergio Menduni,[3,4] Pietro Patimisco,[3] Angelo Sampaolo,[3] Vincenzo Spagnolo,[1,3,a)] and Lei Dong[1,2,a)]

AFFILIATIONS

[1]State Key Laboratory of Quantum Optics and Quantum Optics Devices, Institute of Laser Spectroscopy, Shanxi University, Taiyuan 030006, China
[2]Collaborative Innovation Center of Extreme Optics, Shanxi University, Taiyuan 030006, China
[3]PolySense Lab—Dipartimento Interateneo di Fisica, University and Politecnico of Bari, Via Amendola 173, 70126 Bari, Italy
[4]Photonics Research Group, Department of Electrical and Information Engineering, Politecnico di Bari, 70126 Bari, Italy

[a)]Authors to whom correspondence should be addressed: vincenzoluigi.spagnolo@poliba.it and donglei@sxu.edu.cn

ABSTRACT

Infrared laser technology over the last decades has led to an increasing demand for optical detectors with high sensitivity and a wide operative spectral range suitable for spectroscopic applications. In this work, we report on the performance of a custom quartz tuning fork used as a sensitive and broadband infrared photodetector for absorption spectroscopy. The photodetection process is based on light impacting on the tuning fork and creating a local temperature increase that generates a strain field. This light-induced, thermoelastic conversion produces an electrical signal proportional to the absorbed light intensity due to quartz piezoelectricity. A finite-element-method analysis was used to relate the energy release with the induced thermal distribution. To efficiently exploit the photo-induced thermoelastic effects in the low-absorbance spectral region of quartz also, chromium/gold layers, acting as opaque surface, have been deposited on the quartz surface. To demonstrate the flat response as photodetectors, a custom tuning fork, having a fundamental resonance frequency of 9.78 kHz and quality factor of 11 500 at atmospheric pressure, was employed as photodetector in a tunable diode laser absorption spectroscopy setup and tested with five different lasers with emission wavelength in the 1.65–10.34 μm range. A spectrally flat responsivity of $\sim$2.2 kV/W was demonstrated, corresponding to a noise-equivalent power of 1.5 nW/$\sqrt{Hz}$, without employing any thermoelectrical cooling systems. Finally, a heterodyne detection scheme was implemented in the tunable diode laser absorption spectroscopy setup to retrieve the resonance properties of the quartz tuning fork together with the gas concentration in a single, fast measurement.

I. INTRODUCTION

Trace gas sensing finds applications in numerous fields, such as environmental monitoring,[1] industrial process control,[2] and medical diagnosis.[3] In these applications, a fast and accurate measurement of trace gas concentrations is often required. Optical gas detection using direct absorption spectroscopy is based on the application of the Lambert–Beer law, which relates the optical power transmitted through a gas cell with the incident optical power and the absorption coefficient of the gas sample. Many chemical gas species exhibit strong absorption features in the near- and mid-infrared spectral regions.[4]

The infrared absorption lines or bands are specific to each gas species, and this forms the basis for their selective and accurate detection with narrow linewidth light sources. The commercialization of distributed-feedback (DFB) laser diodes as well as of heterostructure-based lasers (interband and quantum cascade lasers) has revolutionized the field of spectroscopy in the near- and mid-IR range, providing a large quantity of sources capable of covering the whole infrared range in a short time. These sources provide narrow linewidth as well as narrow spectral tunability, thus mostly limiting their use for targeting a single, interference-free absorption line. Indeed, in tunable diode laser

absorption spectroscopy (TDLAS), the emission wavelength of a narrow linewidth laser diode is scanned across an individual gas absorption line and the absorption feature can be fully retrieved.[5] However, DFB lasers do not represent the optimal choice for broadband detection. Although great strides have been made to widen the emission bandwidth of high-power infrared lasers by using, for example, an external cavity (available in the market) or by realizing an array of quantum cascade lasers monolithically grown on a single semiconductor chip,[6] progresses in photodetection are bogged down by the difficulty of obtaining high responsivity over a wide spectral range with a single photosensitive element. Indeed, commercially available photodetectors (PDs) used for sensing different wavelength regions are usually composed of separate photoactive semiconductors, for example, silicon (400–1100 nm), InGaAs (800–1600 nm), and HgCdTe (3–10 μm). The market of near- and mid-infrared PDs is dominated by Thorlabs' amplified PDs and thermoelectrically cooled Vigo detectors, respectively, which offer high responsivity but in a narrow spectral range of operation. Despite great achievements in the field of two-dimensional (2D) material-based photodetection, obvious disadvantages, such as low optical absorbance and instability, preclude their usage for broadband photodetectors with high performance.[7] For example, graphene has been demonstrated to be a promising material for infrared broadband photodetectors due to its gapless band structure,[8] but the low optical absorption of graphene limits its responsivity to the mA/W scale, due to the small optical absorption of a monolayer of carbon atoms. Integration of colloidal quantum dots in the light absorption layer can improve the responsivity of graphene photodetectors, but the spectral range is reduced because light absorption occurs in the quantum dots.[9] Black phosphorus can detect light in both visible and infrared bands due to its tunable bandgap from 0.3 to 1.5 eV, but its environmental instability is a disadvantage.[10] An alternative approach is to find promising 2D materials and fabricate heterojunction structures for multifunctional hybrid photodetectors.[11] However, these technologies are far from reaching commercial maturity. A commercially available quartz tuning fork (QTF) was used to detect electromagnetic radiation—the modulated incident light impacts on QTF prongs, which in turn are put into oscillation.[12] This light detection scheme can occur in principle for all wavelengths of the incident radiation, making the detector potentially suitable for sensing from ultraviolet to far-infrared regions.[13–15] Recently, Ma *et al.*[16] proposed a QTF as a photodetector in a TDLAS setup by focusing the laser light exiting from an absorption cell directly on a QTF. The portion of light absorbed by the QTF generates a deformation due to thermoelastic conversion. A modulation of the optical power causes periodic heating/cooling, which in turn generates a modulation of accumulated charges on the QTF surface due to quartz piezoelectricity. This technique combined with the TDLAS approach, known as light-induced thermoelastic spectroscopy (LITES), has been explored in the last two years. The study of LITES signal as a function of the QTF resonance properties led to the realization of a custom QTF with optimized performance when used as photodetector in a TDLAS setup.[17] Zhang *et al.*[18] demonstrated a linear relationship between the incident optical power and LITES signal without saturation when the LITES signal varies by four orders of magnitude. Xu *et al.*[19] extended the LITES technique in the mid-IR spectral range. To analyze, quantify, and compare the performance of LITES with that of commercially available as

well as state-of-the-art photodetectors, it is essential to measure their figures of merit. Moreover, for broadband application, their spectral dependence in the infrared range has also to be evaluated. QTFs as light detector and have been preivoously demonstrated in several TDLAS setups. These experiments are indicative of QTFs potentiality for a flat and broad detection capability, but no experimental evidences have been provided. A demonstration of these QTFs potentiality requires an in-depth understanding of photo-induced thermoelastic phenomena occurring in the quartz when irradiated by a monochromatic, infrared source. A model of the photo-induced spatial thermal distribution in the area where the light hits the QTF becomes necessary to relate the local temperature increase with the light absorption within the quartz.

In this work, the induced photothermal processes and the temperature distribution corresponding to the absorption of electromagnetic energy upon the crystal quartz is studied by using finite-element-method analysis with COMSOL Multiphysics. The electromagnetic energy release as well as the induced thermal distribution will be related to the absorbance curve of the quartz crystal. In the highly absorbing spectral region, the energy is confined in depths of few tens of micrometers in the quartz crystal. In the low-absorbance spectral region, a deposition of a chromium film and a highly reflective gold layer trap the electromagnetic energy at the quartz/chromium interface, thanks to the strong absorption of chromium in the infrared spectral range, acting as an opaque surface. Thus, a QTF will be realized with an uncoated front surface and a chromium/gold layer-coated back surface, where the light is supposed to be focused. The spectral dependence of two main figures of merit, namely, the responsivity and the noise-equivalent power, of the QTF photodetector will be measured by realizing a TDLAS setup with five interchangeable single-mode DFB laser sources covering the infrared range, from 1.6 to 10.5 μm. Finally, the LITES technique will be combined with a heterodyne detection scheme to simultaneously measure the resonance properties of the QTF as well as the target gas concentration in the absorption cell.

II. T-SHAPED QUARTZ TUNING FORK

By focusing the light onto the QTF prong's clamped end (where the maximum strain should occur), the portion of light absorbed by the QTF creates a local heat accumulation, which causes increase in the local temperature and nearby a strain field nearby proportional to the thermal expansion coefficient of quartz. As a result, this light-induced, thermoelastic conversion occurring in the QTF produces an electrical signal proportional to the absorbed light intensity because of the piezoelectricity of quartz. Each phenomenon contributes to the signal generation. In this way, when the QTF is illuminated, the LITES signal is proportional to the intensity of the strain field (elasticity) generated in the area where the beam is focused, and to the accumulation time in units of heating period (thermic effect), proportional to the ratio between the QTF quality factor and the resonance frequency.[20] When the QTF is excited at one of the flexural modes, the distribution of the strain field as well as the resonator accumulation time depends on the prong geometry.[21] With the QTF placed parallel to the focal plane of the laser beam, the LITES signal follows the intensity distribution of the strain field if the light is modulated at the QTF resonance frequency. However, the areas where the maximum strain occurs lie

on the internal side of the junction between the prong and the support, not on the QTF plane, as sketched in Fig. 1(a).

The research of the maximum strain requires a tilt of the QTF with respect to the beam direction. In Ref. 20, the LITES signal was investigated by using a set of six QTFs with different geometries and its dependence on the product of the strain and the QTF accumulation time was demonstrated. In addition, lowering the pressure within the housing where the QTF is placed, the Q-factor increases and hence the QTF signal follows the same trend. The T-shaped QTF with carved prong surfaces, labeled as QTF#2 in Ref. 20 and hereafter as T-QTF, showed the highest LITES signal. With respect to QTFs with standard rectangular prongs, a T-shaped geometry with a carved surface prong allows the reduction of the resonance frequency and electrical resistance, while retaining a high quality factor, and is thus beneficial for long-duration energy storage.[22] In addition, the mass added on top of each prong results in an increase in the strain intensity close to the QTF prong's clamped end.

As a first step, the T-QTF resonance curve at atmospheric pressure was evaluated. A function generator was used to provide a sinusoidal voltage as excitation signal to the QTF and the output voltage was demodulated by a lock-in amplifier at the same excitation frequency. By varying the excitation frequency step-by-step, the resonance curve was reconstructed. The obtained data are reported in Fig. 1(b). The QTF exhibits an asymmetric behavior in its frequency response due to parasitic capacitance.[23] By imposing a Lorentzian fit, a resonance frequency of 9783.9 Hz and a quality factor Q of $\sim$11 500 at atmospheric pressure were estimated.

III. PHOTO-INDUCED THERMAL EFFECTS IN QUARTZ CRYSTAL

The crystalline α-quartz is Z-cut with a 2° rotation along the X axis, where the Z axis is the optical axis of the crystal and is orthogonal to the plane containing the Z-cut. The bandgap of α-quartz is direct at the Γ point with a magnitude 6.3 eV[24] leading to a high transmission band with a sharp band edge at 0.2 μm. Moving toward lower energies toward the infrared spectral range, the quartz is supposed to be transparent until the first high absorption vibrational modes peak at 1240 cm^{-1} (A2–4-LO), 1163 cm^{-1} (E8-TO), and 1064 cm^{-1} (E7-TO).[25] A transmittance spectrum of 0.75 mm-thick Z-cut α-quartz over a wavelength range of 1–11 μm was measured by using a Nicolet model Fourier transform spectrometer and is shown in Fig. 2.

A high transmissivity ($>$90%) was measured in the spectral range 1–3.5 μm, then it rapidly decreased in the range 3.5–4.8 μm. The narrow absorption features at 2.7 and 4.2 μm are due to water vapor and carbon dioxide absorption, respectively. The low-energy edge of the transmissivity band is determined by the thickness of the sample as well as the optical absorption coefficient. For wavelengths higher than 4.8 μm, the transmissivity reaches values close to zero. The spectral dependence of absorbance reflects that of the optical absorption coefficient: at $\lambda > 4.8$ μm, almost all the electromagnetic energy is deposited in the sample and can generate local heating. Conversely, at $\lambda < 4.8$ μm, light passes through the entire quartz sample and the energy deposited was not sufficient to efficiently stimulate thermoelastic effects. To achieve a high thermoelastic conversion efficiency in the whole infrared spectral range, the corresponding back area [see Fig. 1(a)] was coated with dielectric/metallic films composed of a 50 Å-thick chrome film and a 250 Å-thick gold layer. The real (n) and imaginary (k) parts of the refractive index as well as the optical absorption coefficient of quartz and chromium at the selected wavelengths are listed in Table I.[26–28]

Chromium exhibits a strong absorption band in the mid-infrared range, and it is an excellent adhesion promoter between quartz and gold. With linearly polarized light and near vertical incidence, the Fresnel equations predict a reflection coefficient of $\sim$0.2 at the quartz–chromium interface. The remaining light passes through the chromium to be back-reflected at the chromium–gold interface: with a
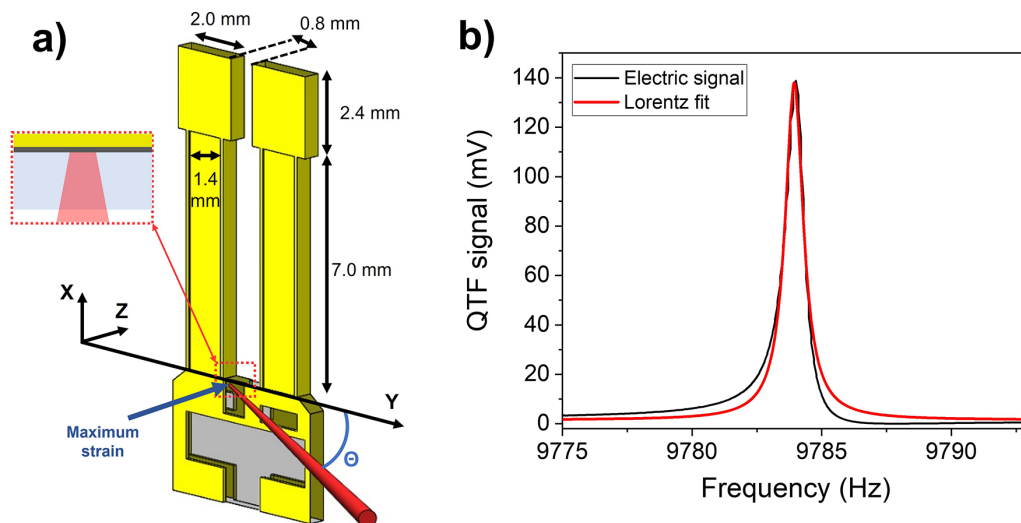

FIG. 1. (a) Schematic of the custom QTF employed in this work with its dimensions. The tuning fork is characterized by a T-shaped geometry and by the presence of 50 μm-deep grooves, carved on the prongs' surface. The incident laser beam (red cone), pointing toward the region of the QTF characterized by maximum strain, is also shown. Inset shows the top-view section of the area in a dashed red box: a 250 μm-thick slice of quartz (light blue), a 50 Å-thick chrome layer (dark gray), and a 250 Å-thick gold layer (yellow). (b) QTF resonance curve acquired at a pressure of 760 Torr (black solid line) and its best Lorentzian fit (red solid line).
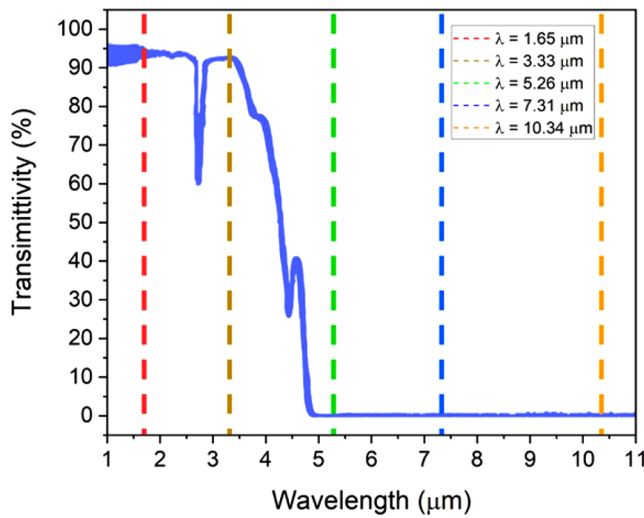
FIG. 2. (Continuous line) transmittance spectrum of the QTF quartz measured using a Fourier transform spectrometer. A 750 μm-thick quartz slab was employed for the measurement. The narrow absorption features around 2.7 and 4.2 μm are due to H_2O and CO_2 absorption, respectively. Schematic representation of the central laser emission wavelengths employed in this work—the dashed lines indicate the selected wavelengths: $\lambda = 1.65\,\mu$m, $\lambda = 3.33\,\mu$m, $\lambda = 5.26\,\mu$m, $\lambda = 7.31\,\mu$m, and $\lambda = 10.34\,\mu$m.

round trip of 100 Å in the chromium layer, the Lambert–Beer law predicts an attenuation of the incident light of ~80%. Thus, it is reasonable to assume that after a second round trip, the light is completely absorbed within the chromium layer. Thereby, when the laser beam with $\lambda < 4.8\,\mu$m is focused on a quartz surface, almost all of it is transmitted through the 250 μm-thick quartz crystal slab and then energy is deposited on the chrome–quartz interface on the back [see Fig. 1(a)]. With these conditions, the induced photothermal processes have been modeled by using a finite-element-method (FEM) analysis. The temperature distribution $T(\mathbf{r}, t)$ related to the absorption of electromagnetic energy upon the elastic body was simulated by using the software COMSOL Multiphysics. The simulation was set up considering a circular quartz slab with a thickness of 250 μm. "Silica Glass" from the COMSOL library was used as the material. The slab is initially at a uniform room temperature and is assumed to be homogeneous and isotropic; the physical and optical properties are assumed to be independent of temperature. Also, the ambient temperature is

TABLE I. Refractive indices and absorption coefficients of quartz and chromium at the wavelengths employed in this work.[26–28]

λ (μm)	Quartz			Chromium		
	N	k	α (cm^{-1})	n	k	α (cm^{-1})
1.65	1.4421	2.00×10^{-5}	1.523	4.2032	5.1494	3.92×10^5
3.33	1.4125	1.90×10^{-4}	7.170	3.5496	10.306	3.89×10^5
5.26	1.3317	9.17×10^{-4}	21.911	3.8524	16.995	4.06×10^5
7.31	1.213	0.00759	130.5	5.0341	24.046	4.13×10^5
1.34	2.4041	0.12405	1507.6	7.8729	33.895	4.12×10^5

assumed to be constant at 294 K. No thermal sources or sinks are supposed to exist within the slab. With high isotropy on a circular surface, only a quarter of the slab was considered, for ease of understanding. The Silica Glass is characterized by a density ρ of 2650 kg/m^3, a thermal conductivity K of 1.38 W/(m·K), and a specific heat C at a constant pressure of 740 J/(kg·K). Two physics modules were combined for the simulation: "radiative beam in absorbing medium"—to simulate the interaction between the incident laser and the quartz slab—and "heat transfer in solids" to simulate the heat propagation in the slab. The latter is based on the generalized hyperbolic thermoelastic model, which admits a finite speed for the propagation of thermal signals, proposed by Lord and Shulman.[29] The light absorption occurring in the chromium/gold coating deposited on the back surface of the QTF was simulated as an opaque surface added on the back side of the quartz slab. The opaque surface absorbs all the incident radiation so that the radiative intensity transmitted beyond the surface is equal to zero. The absorbed intensity was used as a boundary heat source. As a result, the slab is thermally insulated on the bottom face, and subjected to electromagnetic radiation at the upper face. The spatial distribution of the incident beam was modeled with a Gaussian profile having a full-width-half-maximum value of 200 μm. The incident power was set to 5 mW. The laser beam is focused along the z-direction, hitting the upper surface of the quartz slab at coordinates (0,0,0). The radiation crosses the interface and is then absorbed by the medium. This point is the corner of a quarter of the slab, and it resembles the edge of the prong–support junction in the (x, y) plane, where the maximum strain occurs when the laser beam is aligned to the z-direction. To evaluate the distribution of temperature at different wavelengths, i.e., 1.65, 3.33, 5.26, 7.31, and 10.34 μm, the refractive index (the real part n and the imaginary part k) and absorption coefficient of quartz listed in Table I have been used. The simulation was carried out in a stationary regime. This condition was verified to be reached after ~120 s. The three-dimensional temperature distribution (the quarter of quartz slab with a light yellow-to-orange color palette) as well as the energy intensity distribution (represented by an ideal small quarter of slab with blue-to-red color palette and sketched adjacent to the quartz slab) is shown in Fig. 3 for these selected wavelengths.

The radiative intensity distribution along the z-direction (at $x = 0$ and $y = 0$) is reported in Fig. 4(a) for all the selected wavelengths.

For highly absorbing wavelengths, $\lambda = 7.31$ and $10.34\,\mu$m, the energy absorption occurs in a region of finite and small thickness near the surface. An electromagnetic skin depth, i.e., the value of z at which the laser power is $1/e$ times its maximum (surface) value, can be extracted to be 76 and 7 μm for $\lambda = 7.31$ and $10.34\,\mu$m, respectively. Figure 4(b) displays the calculated temperature distribution in the z-direction (at $x = 0$ and $y = 0$). Slab surface temperatures are always higher than the ambient air temperatures and nonlinear temperature gradients are predicted across the slab. In particular, for highly absorbing wavelengths, a localized heating accumulation on surface $z = 0$, i.e., the surface where the beam is focused, can be predicted. For weakly absorbing wavelengths, $\lambda = 1.65$, 3.33, and 5.26 μm, the radiation passes through the 250 μm-thick quartz slab and is completely absorbed by the opaque surface on the back, which simulates the chrome/gold layers. As a result, the temperature gradient along the z-direction is opposite in sign with respect to highly absorbing wavelengths, causing a localized heating accumulation on surface $z = 250\,\mu$m. Figure 4(c) shows the temperature distribution along the
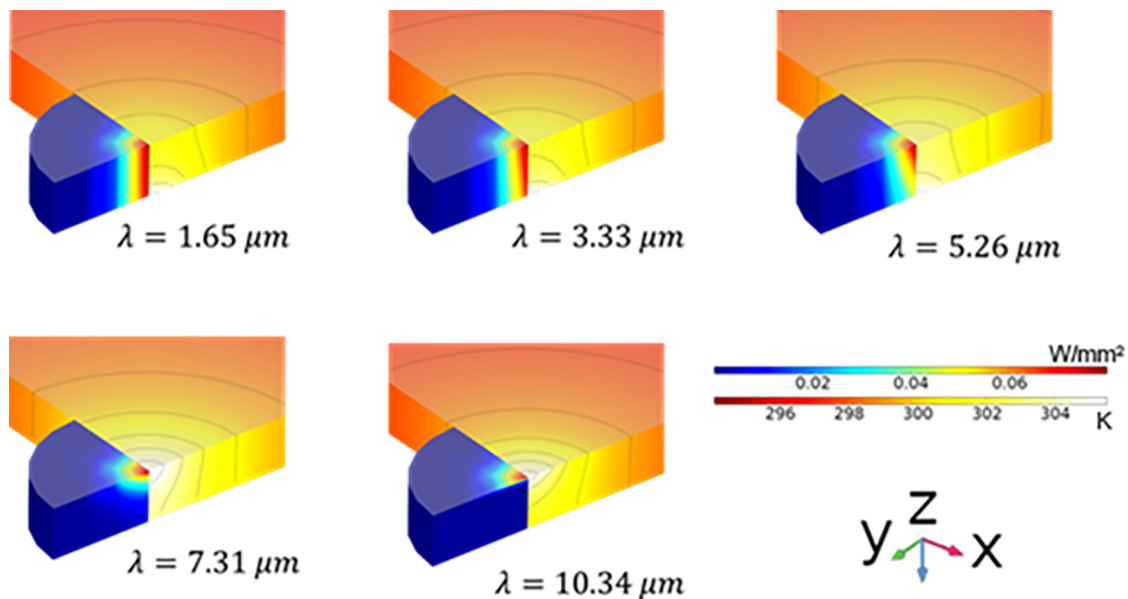
FIG. 3. COMSOL Multiphysics finite-element-method (FEM) simulation of the spatial distribution of both the radiative intensity (rainbow color scale) and temperature (heat color map) for a 250 μm-thick quartz slab, as a result of laser beam absorption. For ease of comprehension, only a quarter of the quartz slab is represented here, and the heat color map representing the temperature is superimposed onto this region. The rainbow color scale is represented adjacent to the quartz slab. Laser beam hits the quartz on its upper surface and then propagates downward, along the z axis.

x-direction, perpendicular to light incidence along the z-direction. As discussed above, the temperature distribution is reported for the incidence plane ($z = 0$) for $\lambda = 7.31$ and $10.34\,\mu$m, and for the backside plane ($z = 250\,\mu$m) for the other wavelengths. The results show that the broadening of the temperature distribution on the (x, y) plane is not wavelength-dependent. This indicates that an opaque surface allows the achievement of the same thermal conditions on quartz backside for non-absorbing wavelengths as those achievable on the incidence plane for highly absorbing wavelengths. In Fig. 4(d), the surface temperature (the plane $z = 0$ for $\lambda = 7.31$ and $10.34\,\mu$m and the plane $z = 250\,\mu$m for $\lambda = 1.65$, 3.33, and $5.26\,\mu$m) has been simulated as a function of the incident power, with all other parameters fixed. The surface temperature scales linearly as a function of the incident power with slopes weakly varying with the wavelength (from 2.06 k/mW at 7.31 μm, to 2.51 K/mW at 10.34 μm). In conclusion, for weakly absorbing wavelengths, an opaque surface on the backside should retrace the same thermal conditions that are achievable at the top surface when high-absorbing light hits it. These simulation results are very promising in terms of a wavelength-independent photo-induced thermoelastic conversion within the quartz over the entire infrared range.

IV. EXPERIMENTAL SETUP

The experimental setup for LITES configuration is sketched in Fig. 5.

A stainless steel housing (SSH) equipped with two interchangeable windows was employed to accommodate the T-QTF. A vacuum pump and a pressure controller were connected to the housing to maintain the internal pressure at 5 Torr. A constant flow of pure N_2

was purged inside the housing to avoid interference from the analytes in the environment. The housing was fixed to a three-axis translation stage, equipped also with two angular degrees of freedom, which allowed fine tilt/adjustments of the QTF position with respect to the laser beam. The laser beam passes through an absorption cell containing the target gas and is then focused on the T-QTF through a lens with a focal length of 50 mm. Five different lasers were selected to analyze the QTF performances. The list of laser sources and related target gases is shown in Table II. For each laser reported in Table II, a gas absorption cell was filled with a gas mixture containing a fixed concentration of target gas and nitrogen as balance gas, at the atmospheric pressure, except NH_3 where the mixture pressure in the cell was fixed to 70 Torr. Table II resumes the employed experimental conditions. The selected absorption lines are reported together with the corresponding absorption cross sections and gas target concentrations. The absorption cross sections were retrieved by using the HITRAN database and simulating a mixture containing the gas target concentration in a nitrogen mixture, at the operating pressure.[30] The optical pathlengths are also reported.

For each wavelength, the cell and housing windows, as well as the focusing lens, were properly selected to provide high transmittance and anti-reflection coating and maximize the portion of light that impacts on the T-QTF. The laser current was modulated at half of the T-QTF resonance frequency while the QTF signal is collected by means of a preamplifier and then demodulated at the resonance frequency by means of a lock-in amplifier, in wavelength modulation and *2f*-detection (WM-2f) approach. A slow triangular ramp is also applied to the current driver to linearly scan the laser wavelength across the selected absorption line.
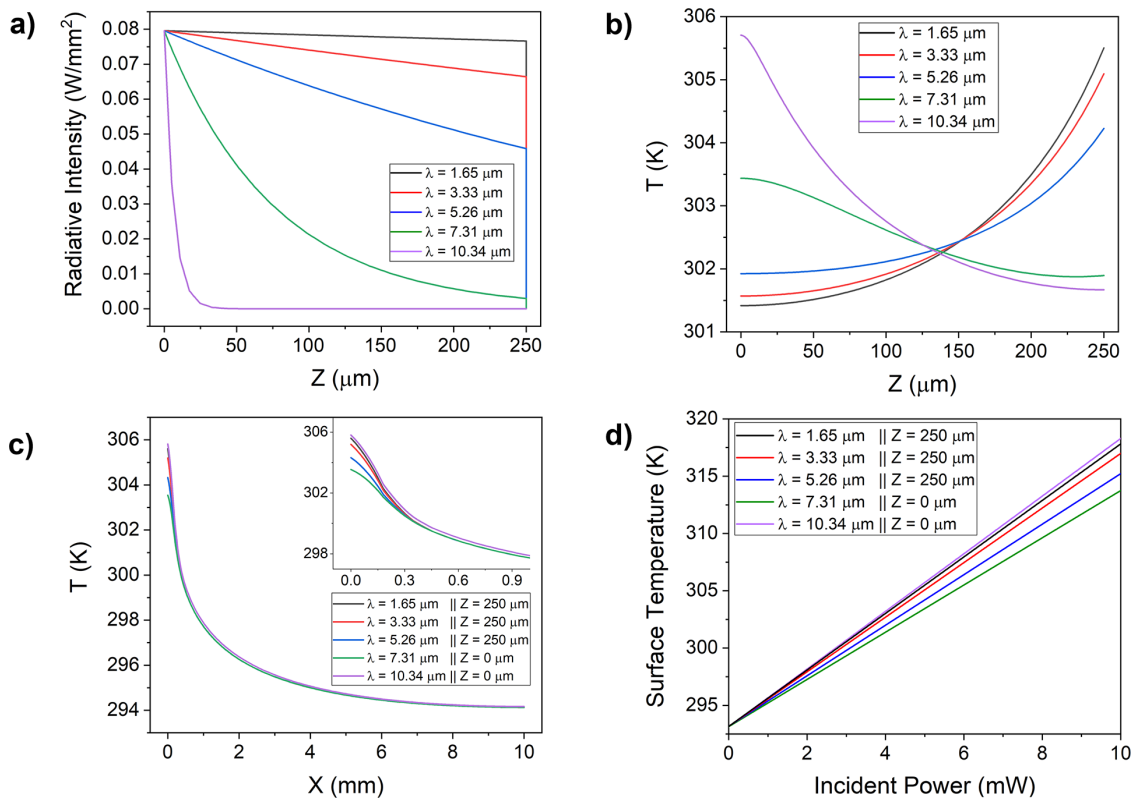
FIG. 4. Results of COMSOL Multiphysics simulation. (a) Radiative intensity distribution along the z axis at beam incidence location ($x = 0$ and $y = 0$) for the selected wavelengths. (b) Temperature distribution along the z axis at beam incidence location ($x = 0$ and $y = 0$) for the selected wavelengths. (c) Temperature distribution along the x axis on the incidence plane ($z = 0$) for $\lambda = 7.31$ and $10.34\ \mu m$, and on the backside plane ($z = 250\ \mu m$) for $\lambda = 1.65, 3.33$, and $5.26\ \mu m$. Inset shows a zoom in the range 0–1 mm to better discriminate the temperature around $x = 0$. (d) Surface temperature as a function of laser incident power, on the incidence plane for $\lambda = 7.31$ and $10.34\ \mu m$, and on the backside plane for $\lambda = 1.65, 3.33$, and $5.26\ \mu m$, at the point (0,0).
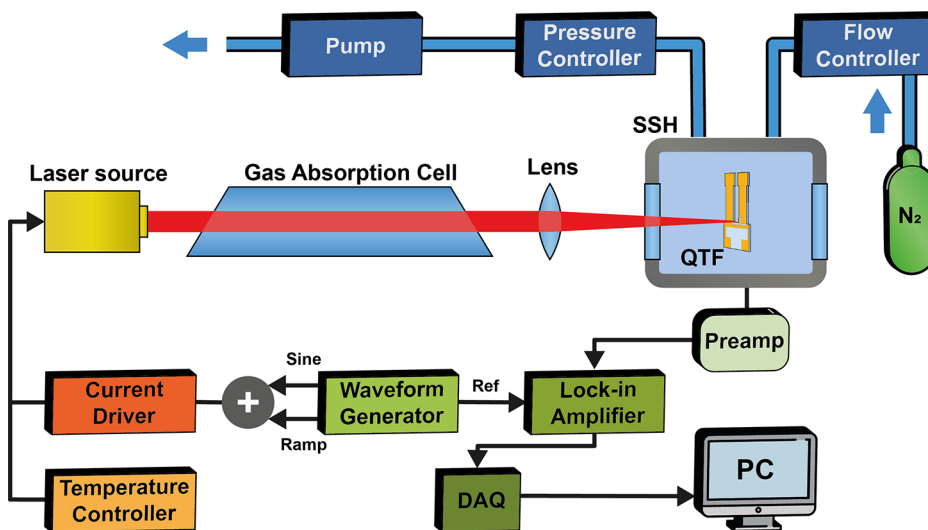

FIG. 5. Sketch of the employed experimental setup. In the upper part of the schematic design, the gas line management system is represented (blue blocks). In the lower part of the schematic design, both the laser control units (orange blocks) and the instruments devoted to signal demodulation and acquisition (green blocks) are represented. QTF: quartz tuning fork; SSH: stainless steel housing; DAQ: digital acquisition; and PC: personal computer.

TABLE II. Main features of the laser sources and target gases used for LITES and H-LITES analysis. *: multipass cell; LD: laser diode; ICL: interband cascade laser; QCL: quantum cascade laser; and EC: external cavity.

Laser sources			Gases to be detected			Absorption cells
Laser type	Wavelengths (μm)	Power (mW)	Gas target	Concentration (%)	Cross section (cm^2/molecule)	Pathlength (cm)
LD	1.65	1.13	CH_4	0.5	7.40×10^{-23}	1000*
ICL	3.33	1.2	CH_4	1	3.11×10^{-21}	15
QCL	5.26	5.1	H_2O	1	2.23×10^{-23}	60
EC-QCL	7.31	3.6	H_2O	1	3.74×10^{-22}	60
QCL	10.34	5.6	NH_3	0.024	3.97×10^{-21}	15

V. SPECTRAL RESPONSIVITY AND NOISE EQUIVALENT POWER

Following the scheme reported in Table II, the spectral scan of each selected absorption line was acquired by using the experimental setup reported in Fig. 5 operated in the WM-2f approach, by interchanging the laser source with the appropriate gas absorption cell.

Each spectral scan resembles the second derivative of a Lorentzian line shape, as expected when the WM and 2f-detection approach is adopted, meaning that single, well-isolated absorption lines are targeted without spectral neighbor interference features. The asymmetry of negative lobes is a result of residual amplitude modulation, coming from the modulation of optical power.[31] The LITES signals can be used to estimate the responsivity of QTF-based photodetectors for each wavelength investigated. The voltage spectral responsivity is defined as the output signal response to monochromatic radiation at a frequency υ incident on a photodetector. When the light is modulated at a frequency f, the voltage responsivity $R_V(\nu, f)$ can be expressed as

$$R_V(\upsilon, f) = \frac{S_V(f)}{\Delta P(\upsilon)}, \qquad (1)$$

where $S_V(f)$ is the voltage signal due to an optical power modulation ΔP. When the photodetector is used in direct absorption with the WM and 2f-detection approach, the incident power is modulated with a small sinusoidal dither at f and the second harmonic component is extracted from the photo-generated electrical signal. With low modulation index and weak optical absorption, the 2f-component ΔP_{2f} of an f-modulated optical power transmitted by an absorbing sample after a path length L can be extracted through a Taylor series expansion. At the absorption peak υ_0, ΔP_{2f} can be expressed as[32]

$$\Delta P_{2f}(\upsilon_0) = \frac{P_0}{4} \alpha''(\upsilon_0) \Delta \upsilon^2 L, \qquad (2)$$

where P_0 is the continuous component, $\alpha''(\upsilon_0)$ is the second derivative of the absorption line, and $\Delta \upsilon$ is the frequency modulation. Assuming a Lorentzian shape for the absorption coefficient,

$$\alpha(\upsilon) = \sigma(\upsilon)N = \frac{SN\gamma}{\pi[(\upsilon - \upsilon_0)^2 + \gamma^2]}, \qquad (3)$$

the second derivative calculated in $\nu = \nu_0$ can be expressed as

$$\alpha''(\upsilon_0) = -\frac{2\sigma(\upsilon_0)N}{\gamma^2}, \qquad (4)$$

where S is the line strength of the radiative transition; $\sigma(\upsilon_0)$ is the absorption cross section at the absorption peak; γ is the Half Width Half Maximum (HWHM) of absorption line; and $N = PN_A/(RT)$ is the molecular density estimated by using the ideal gas law (R is the gas constant, N_A is the Avogadro number, P and T are the gas pressure and temperature, respectively). In the WM–2f approach, the peak signal is maximized when the modulation depth $\Delta \upsilon \sim \gamma$. By imposing this condition and combining Eqs. (2)–(4), the 2f-component of the optical power modulation can be estimated, and the responsivity calculated by using Eq. (1) and peak values S_V extracted by the spectral scans plotted in Figs. 6(a)–6(e). All these parameters are listed in Table III, for each wavelength investigated.

In Fig. 7, the spectral dependence of responsivity is reported for the T-QTF, together with the most performant and broadband Thorlabs photodetector (model PDA10CF), and for three broadband Vigo infrared photodetectors, as provided by datasheets.

PDA10CF is confined to operate in a narrow spectral range while Vigo detectors require three different designs (PVI-4, PVI-6, and PVI-10.6, where the last digits represent the optimal operating wavelength) to cover the whole mid-infrared range with the disadvantage that the broader the spectral band, the lower is the responsivity. The T-QTF photodetector can cover the whole infrared spectral range with a flat spectral response, as predicted by the theoretical model described in Sec. III, resulting in an excellent compromise between broadband operation and high-level responsivity.

Responsivity does not consider the level of total intrinsic noise of the photodetector. The noise-equivalent power (NEP) is the common metric that quantifies a photodetector's ultimate sensitivity as the power generated by a noise source. It is defined as the signal power that gives a signal-to-noise ratio of one in a 1 Hertz-output bandwidth:

$$NEP = \frac{S_N}{R_\nu}, \qquad (5)$$

where S_N is the noise spectral density. The QTF preamplifier employed is constituted by two stages: a transimpedance amplifier with a feedback resistor R_f and a voltage amplifier with a gain of 30. Assuming that the voltage amplifier does not contribute as noise source, the QTF noise measured at the amplifier output at the resonance frequency is primarily determined by the thermal noise of the QTF resistance R_{QTF} and of the feedback resistor R_f. However, the feedback resistor introduces noise that is several times lower than the thermal QTF noise because R_f typically is in the MΩ range, several times higher than R_{QTF}, which varies in in the range 10–100 KΩ. As a result, the ultimate noise spectral density is the thermal noise of the QTF:
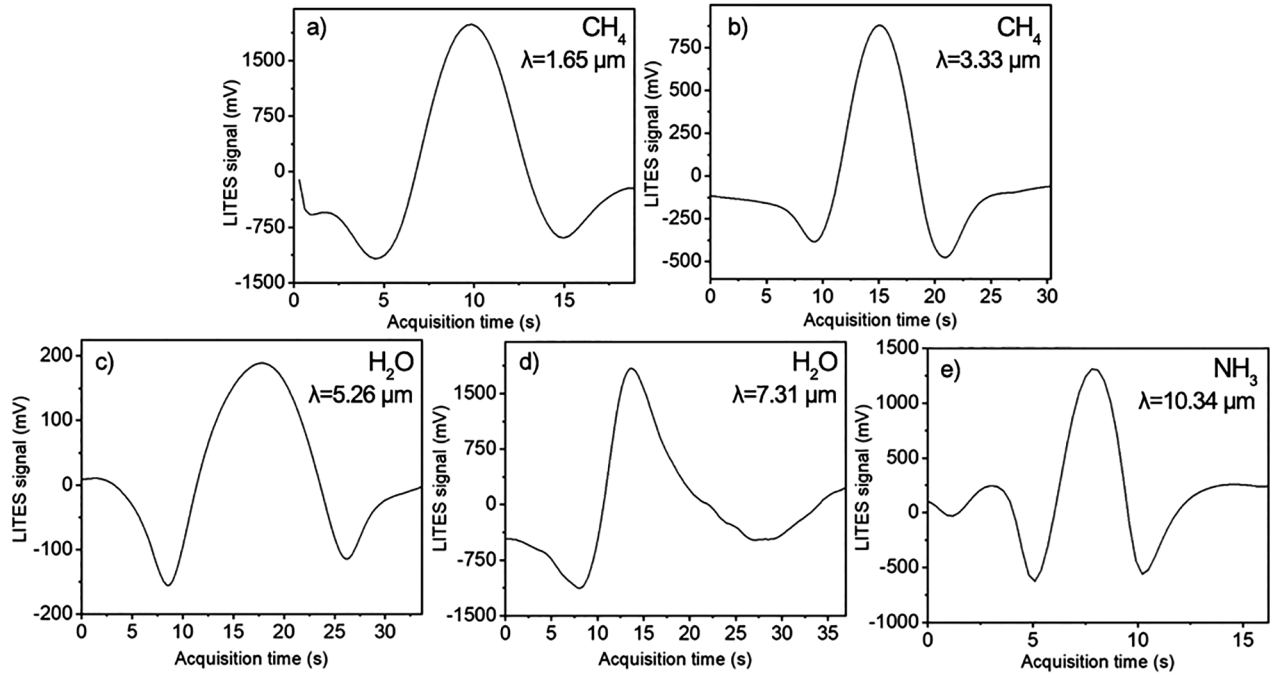
FIG. 6. (a) LITES signal acquired as a function of the acquisition time required to scan across the methane absorption line peaked at 6057.09 cm^{-1}; (b) LITES signal acquired as a function of the acquisition time required to scan across the methane absorption line peaked at 2998.99 cm^{-1}; (c) LITES signal acquired as a function of the acquisition time required to scan across the water absorption line peaked at 1901.76 cm^{-1}; (d) LITES signal acquired as a function of the acquisition time required to scan across the water absorption line peaked at 1368.63 cm^{-1}; and (e) LITES signal acquired as a function of the acquisition time required to scan across the ammonia absorption line peaked at 967.35 cm^{-1}.

$$S_n = \frac{\sqrt{\langle V_N^2 \rangle}}{\sqrt{\Delta f_D}} = R_f \sqrt{\frac{4K_B T}{R_{QTF}}}, \qquad (6)$$

where V_N is the voltage noise at the preamplifier output, Δf_D is the detection bandwidth, and $K_B = 1.38 \times 10^{-23}$ J/K is the Boltzmann constant. By using $R_f = 10$ MΩ and $R_{QTF} = 150$ kΩ, the theoretical QTF-based photodetector noise spectral density is $S_n \sim 3.3$ μV/Hz$^{0.5}$. The QTF-based photodetector noise spectral density was experimentally measured by using the setup depicted in Fig. 5 with the laser off, i.e., removing all external excitations for the QTF. Then, the noise was recorded as a function of the frequency by acquiring the QTF signal at different modulation frequencies in a narrow spectral region around the QTF resonance frequency $f_0 = 9783.9$ Hz. The results are shown in Fig. 8.

TABLE III. S_V values extracted by spectral scans plotted in Figs. 6(a)–6(e). ΔP_{2f} values calculated by using Eqs. (2)–(4). Voltage responsivity R_V at five wavelengths estimated by using Eq. (1).

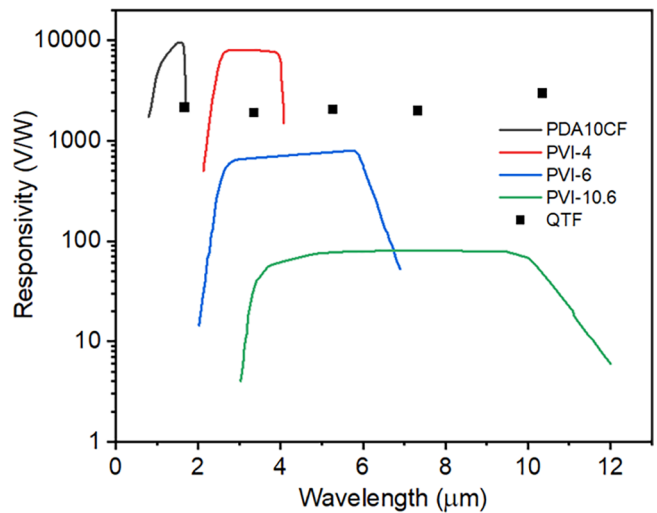| Wavelength (μm)	S_V (V)	ΔP_{2f} (mW)	R_V (V/W)
1.65	1.98	0.918	2160
3.33	0.88	0.458	1920
5.26	0.19	0.091	2090
7.31	1.84	0.911	2020
10.34	1.31	0.437	3000

FIG. 7. Responsivity (represented by solid lines) as a function of the wavelength for three models of photovoltaic Vigo detectors, namely, PVI-4 (red line), PVI-6 (blue line), and PVI-10.6 (green line) HgCdTe, and for Thorlabs PDA10CF InGaAs Amplified Photodetector (black line), as provided by the device manufacturers. Responsivity of the T-QTF (represented by black square) when employed as a photodetector. The data in the graph were calculated employing Eq. (1), as reported in Table III.
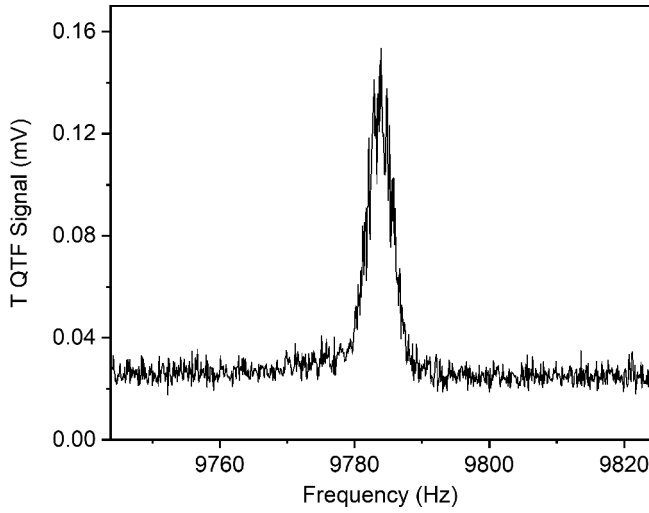
FIG. 8. Noise spectrum of the T-QTF as a function of the operating frequency. The noise spectrum is acquired by performing an electrical characterization of the tuning fork around its fundamental resonance frequency at 9783.9 Hz.

Far from the resonance frequency, the photodetector exhibits a flat electronic noise of $\sim 26\,\mu V$, which increases up to $\sim 135\,\mu V$ at the resonance frequency. By considering the gain factor 30 of the voltage amplifier, i.e., the second stage of the QTF preamplifier, and the lock-in detection bandwidth of 1.67 Hz (filter slope 12 dB/octave), the noise spectral density at f_0 results in $S_n = 3.35\,\mu V/\sqrt{Hz}$. A comparison with the theoretical prediction makes it possible to affirm that the ultimate noise level of the sensor is determined by the thermal noise of the QTF. With a measured averaged responsivity of $R_V \sim 2200$ (see Table III), the NEP can be calculated to be 1.5 nW/$\sqrt{Hz}$ by using Eq. (5), which is an excellent value considering that the QTF operates without any thermo-cooling systems.

VI. HETERODYNE-BASED LIGHT INDUCED THERMO-ELASTIC SPECTROSCOPY

The flat spectral responsivity makes the QTF an excellent candidate as a broadband infrared photodetector. However, the resonance properties of the QTF determine its ultimate performance. Indeed, the LITES signal is proportional to the QTF accumulation time, and the ultimate noise depends on the electrical resistance of the QTF as well as on its temperature. In LITES, a continuous, real-time monitoring of QTF resonance properties is mandatory to ensure that the sensor response is determined only by gas absorption and not by variations of QTF resonance properties. The resonance frequency and Q-factor of a QTF as well as the trace-gas concentration can be simultaneously retrieved by detecting the beat frequency signal generated when the transient response signal of the QTF is demodulated at its non-resonance frequency. This approach was first proposed for QEPAS in Ref. 33 and here is extended to the LITES technique. If a photothermal pulse is focused on the QTF, its prongs will start to vibrate in a short period of time. After the pulse terminates, QTF prongs will dissipate the accumulated energy via loss mechanisms, vibrating at the natural vibrational mode. With the oscillation period of $\sim 100\,\mu s$, the time-dependence of natural oscillations is difficult to record with high temporal resolution. Thus, a heterodyne-based LITES (H-LITES) approach can be adopted by modulating the laser frequency at $f = f_0 + \Delta f$, with $\Delta f \ll f_0$. By using the experimental setup depicted in Fig. 5, a fast pulsed ramp current is added to the laser current driver to rapidly scan across a targeted absorption line while a sinusoidal dither at f is simultaneously applied. The QTF signal is demodulated at f_0 by the lock-in amplifier. As a result, a beat frequency signal between the QTF resonance frequency f_0 and the laser modulation frequency f will be generated. Thus, by recording the demodulated QTF signal as a function of time, a sinusoidal waveform with exponentially decreasing amplitude at a period of $\Delta t = 1/\Delta f$ is expected. By measuring Δt, the resonance frequency f_0 of the QTF can be retrieved. In addition, the exponential decay of peak values of the successive oscillations (envelope function) is related to the Q-factor of the QTF resonance since the Q-factor itself is defined as the ratio of the energy accumulated in the pulsed-excited QTF and the energy loss per cycle. Moreover, the amplitude of the beat signal can be easily related to the absorbing gas concentration. As discussed in Sec. III, the photoinduced heat produces elastic deformation in the quartz sample, i.e., TE strain $\varepsilon_{TE}(z, t)$, proportional to the change of temperature distribution $T(z, t)$ given by

$$\varepsilon_{TE}(z,t) = \alpha_T T(z,t), \tag{7}$$

where α_T is the coefficient of linear thermal expansion, equivalent to that which would be produced by a stress $\sigma(z, t) = E \cdot \varepsilon_{TE}(z, t) = E \cdot \alpha_T \cdot T(z, t)$ applied to the free end of the prong, where E is the Young's modulus. The strain induces a local polarization $p(z, t)$ of quartz and charges appearing on the surface are collected by electrical contacts appropriately deposited along the QTF prong.[21] In the elastic regime, the relation between $p(z, t)$ and $\varepsilon_{TE}(z, t)$ reduces to the scalar expression $p(z, t) = d_{11}\sigma(z, t) = d_{11}E\alpha_T T(z, t)$, where d_{11} is the longitudinal piezoelectric modulus. As a result, the generated piezocurrent will be proportional to the surface temperature; this is in turn proportional to the optical power absorption ΔP_{2f} occurring on the quartz surface [see Fig. 3(d)], which can be related to the absorbing gas concentration by Eqs. (2)–(4). Thus, when irradiated, the modeling of the QTF electrical response can be reduced to an RLC circuit with an ideal current generator in parallel with the QTF electrical resistance, as depicted in Fig. 9.

The preamplifier input is represented by a RC parallel, where R_{ampli} and C_{ampli} are the equivalent input resistance and capacitance of the preamplifier, respectively. The magnitude of the Laplace transfer function relating the QTF generated current with the amplifier input current is described by the following expression as a function of the Laplace variable s:

$$V_0(s) = \left|\frac{I_{ampli}(s)}{I_{QTF}(s)}\right|^2 = \left|\frac{sC_{QTF}R_{QTF}(1 + sR_{ampli}C_{ampli})}{1 + s[R_{ampli}(C_P + C_{ampli} + C_{QTF})] + s^2[L_{QTF}C_{QTF} + R_{ampli}C_{QTF}R_{QTF}(C_P + C_{ampli})] + s^3 R_{ampli}L_{QTF}C_{QTF}(C_P + C_{ampli})}\right|^2. \tag{8}$$
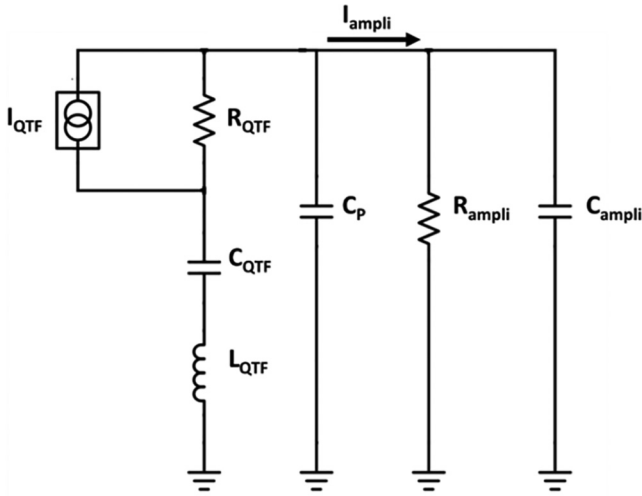
FIG. 9. Schematic of the equivalent circuit of the QTF. R_{QTF}, C_{QTF}, and L_{QTF} are the resistance, the capacitance, and the inductance of the QTF, respectively. C_p is the parallel stray capacitance. R_{ampli} and C_{ampli} are the equivalent input resistance and capacitance of the preamplifier, respectively. I_{QTF} and I_{ampli} are the currents flowing in the QTF and in the preamplifier, respectively.

The electrical parameters of the QTF, namely, R_{QTF}, C_{QTF}, and L_{QTF}, are related to the resonance properties of the QTF by the relations

$$f_0 = \frac{1}{2\pi}\sqrt{\frac{1}{L_{QTF}C_{QTF}}}; \quad Q = \frac{1}{R_{QTF}}\sqrt{\frac{L_{QTF}}{C_{QTF}}}. \quad (9)$$

Considering $R_{ampli} = 1\,k\Omega$, $C_{ampli} = 5\,pF$, $f_0 = 9784.78\,Hz$, and a quality factor $Q = 38\,146$, the normalized QTF transfer function around

the resonance frequency f_0 extracted from the circuit in Fig. 9 is represented by the black curve in Fig. 10(a).

The H-LITES technique can be simulated by assuming a single narrow-width current pulse superimposed by a sinusoidal modulation at frequency f as input source for the circuit in Fig. 9. After the short pulse ($t = 0$), the QTF is free to vibrate in its natural mode at the fundamental resonance frequency f_0. The Q-factor of the natural mode determines the time constant τ_{QTF} of the free-oscillation exponential damping, according to the expression $\tau_{QTF} = Q/\pi f_0$. If the response of the circuit is demodulated at $f = f_0 + \Delta f$, the obtained signal $V_D(t, f)$ after the single short pulse is supposed to oscillate at the beat frequency Δf, with an exponential decay of peak values mainly determined by τ_{QTF}. The integration time constant must be shorter than τ_{QTF}. Assuming $V_D(0, f) = V_0(f)$ the circuit response immediately after the pulse, the demodulated QTF signal can be described by the following expression:

$$V_D(t,f) = V_0(f)e^{-t/\tau_{QTF}}\cos(2\pi\Delta f \cdot t). \quad (10)$$

The beat frequency Δf allows the calculation of the QTF resonance frequency as $f = f_0 + \Delta f$; then, Q can be estimated by measuring τ_{QTF}. The transient response V_D demodulated at $f = 9785.42\,Hz$ ($\Delta f = 0.64\,Hz$) is represented in Fig. 10(b). If the first negative peak is neglected as discussed in Ref. 33, the second peak value can be extracted and plotted for different demodulation frequencies. The results are shown by purple a solid line in Fig. 10(a). The analysis shows the presence of two demodulation frequencies equidistant from f_0 that maximizes the second peak value in Fig. 10(b). Thus, the maximum beat signal is obtained when the detuning frequency is $\Delta f_{MAX} = \pm 0.64\,Hz$.

Following the simulation results, the H-LITES technique was implemented for the detection of a methane absorption line peaked at $6057.09\,cm^{-1}$, by using a laser diode and a 10 m Herriott multipass cell filled with a methane concentration of 0.5% in nitrogen at a pressure of 80 Torr (see Table II). Using the experimental setup in Fig. 5,
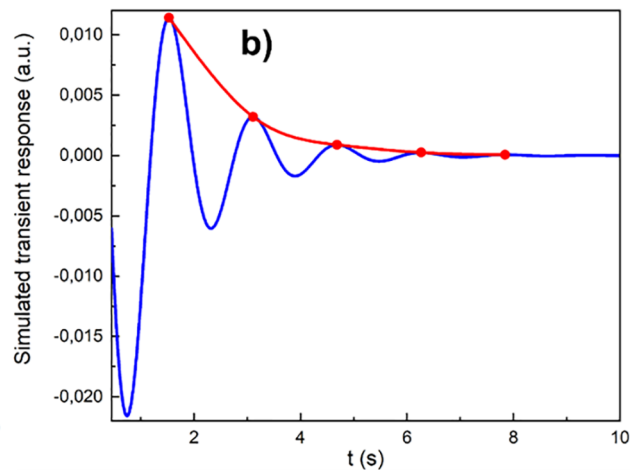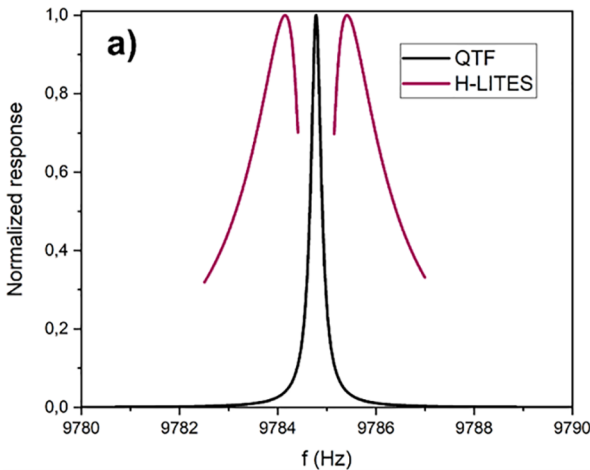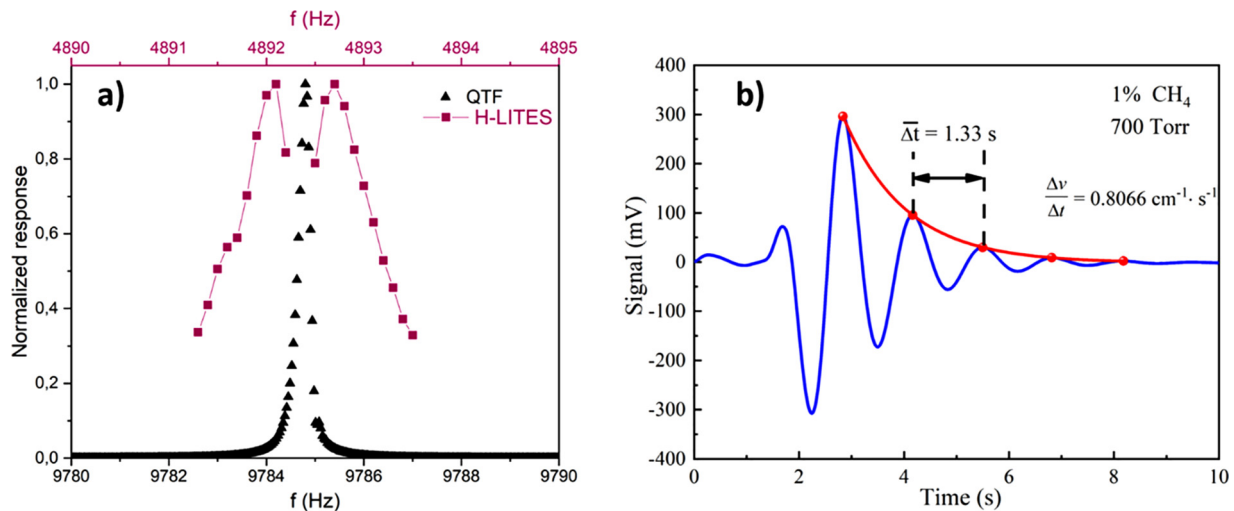

FIG. 10. (a) QTF transfer function of the circuit depicted in Fig. 9. The electrical response of the quartz tuning fork is acquired by performing an electrical characterization of the resonator around the resonance frequency $f_0 = 9784.78\,Hz$ (black solid line). Demodulated circuit response as a function of the demodulation frequency collected by employing the heterodyne-based LITES technique (purple solid line). (b) Transient circuit response demodulated at $f = 9785.42\,Hz$ as a function of time collected by employing the heterodyne-based LITES technique (solid blue line). The red line is the envelope function of positive peak values.

FIG. 11. (a) H-LITES signal as a function of the excitation frequency. Purple square symbols represent the normalized experimental data acquired via the H-LITES technique, while the black triangles represent the QTF electrical characterization. (b) H-LITES as a function of time for a demodulation frequency of 9785.42 Hz ($\Delta f = 0.62$ Hz) is plotted as a blue solid line. The red line is the envelope function of positive peak values.

the laser current driver was sinusoidally modulated at $f/2$ together with a ramp signal with a spectral scan rate of $\Delta\nu/\Delta t \sim 0.807$ cm$^{-1}\cdot$s^{-1} across the targeted methane absorption line. The QTF signal was demodulated at f by the lock-in amplifier and then acquired and recorded as a function of time. Figure 11(a) shows the H-LITES peak signal as a function of the modulation frequency together with the resonance curve of the QTF fundamental mode measured at 80 Torr.

The experimental maximum of the H-LITES signal is obtained when the detuning frequency is $\Delta f = \pm 0.62$ Hz, in excellent agreement with the theoretical prediction. Figure 11(b) shows the H-LITES signal as a function of time when the detuning frequency is $\Delta f = 0.62$ Hz, acquired immediately after the ramp excitation, i.e., when the QTF starts to relax the excess of stored energy vibrating at the fundamental mode. A period of oscillation $\Delta t = 1.33$ s was measured, leading to $f_0 = 9784.95$ Hz, less than 1% different from the measured values of 9784.78 Hz extracted from the QTF resonance curve. The positive peak values for each oscillation were extracted and plotted with an exponential decay function $V_0\exp(-t/\tau_{QTF})$, resulting in $\tau_{QTF} = 1.18$ s and leading to a quality factor $Q = \pi f_0\cdot\tau_{QTF} = 36\,274$. The Q-factor extracted by the resonance curve ($Q = f_0/FWHM$, where $FWHM$ is the full-width half-maximum of the resonance curve) is 38 146. Since the peak value is proportional to the gas concentration,[33] Fig. 12 shows the H-LITES peak signal extracted for different methane concentrations in the multipass cell.

The H-LITES peak signal shows an excellent linear response in the investigated concentration range. A minimum detection limit of 1.5 ppm can be estimated by considering a noise level of 62 μV.

VII. CONCLUSIONS AND PERSPECTIVES

In this work, we demonstrated that a QTF can operate as a narrow-bandwidth ($\sim$1 Hz), fast-response (tens of kHz), broadband, high-responsivity infrared photodetector, suitable for tunable laser-based absorption spectroscopy. The spectral responsivity as well as the noise-equivalent power were measured as a function of wavelength

and compared with the most performant infrared detectors available on the market. We demonstrated an average responsivity of $R \sim 2200$ KV/W, comparable with the commercially available photodetectors, but with the advantage that it is flatly extended across the whole infrared spectral range of 1.65–10.34 μm without requiring any thermoelectrical cooling system. Thus, a QTF photodetector can be suited for use in all gas spectroscopy systems, both for broad- and narrow-band operation, without any loss in responsivity. QTF photodetectors can be easily integrated in a fast Fourier transform
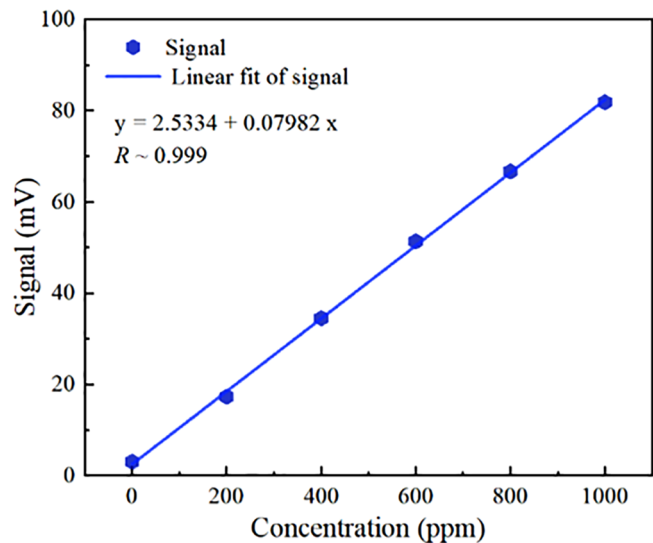

FIG. 12. H-LITES peak signal of the methane absorption line at 6057.09 cm^{-1} as a function of CH$_4$ concentration in the range 0–1000 ppm in nitrogen (blue hexagonal points). The blue solid line is the best linear fit retrieved for the data points shown in the graph.

spectrometer (avoiding the change of detector when varying the spectral range of investigation) as well as in TDLAS sensor systems. This paves the way for realization of a broadband spectrometer to be used as a gas analyzer in an easy configuration that can provide comparable sensitivity of a DFB laser-based TDLAS sensor over a broad spectral band. There are several primary motivations for using broadband spectroscopy as an analytical tool. First and foremost, a large spectral bandwidth allows the simultaneous detection of multiple species. This enables a single instrument to serve many purposes and provides a more complete understanding of complex processes. In addition, a broad bandwidth enables accurate measurements in complex systems, where interfering absorption from unexpected features can cause significant errors for measurements with a limited spectral bandwidth. Moreover, TDLAS can be extended to applications that cannot be covered by standard, narrow-band TDLAS techniques, such as analysis of air composition, breath sensing, and security. In conclusion, our extensive and detailed analysis provides essential guidelines for the technological development of QTF-based light detectors. In addition, our results can inspire the development of novel strategies aimed at enhancing the photo-induced thermal effect occurring in quartz crystals.

ACKNOWLEDGMENTS

AUTHOR DECLARATIONS
Conflict of Interest

The authors declare no conflict of interest.

Author Contributions

T.W. and A.Z. contributed equally to this work.

DATA AVAILABILITY

The data that support the findings of this study are available from the corresponding author upon reasonable request.

REFERENCES

[1]H. I. Schiff, G. I. Mackay, and J. Bechara, Res. Chem. Intermed. **20**, 525–556 (1994).
[2]K. Krzempek, R. Lewicki, L. Nähle, M. Fischer, J. Koeth, S. Belahsene, Y. Rouillard, L. Worschech, and F. K. Tittel, Appl. Phys. B **106**, 251–255 (2012).
[3]R. Ghorbani and F. M. Schmidt, Opt. Express **25**, 12743–12752 (2017).
[4]J. Hodgkinson and R. P. Tatam, Meas. Sci. Technol. **24**, 012004 (2013).
[5]L. Dong, F. K. Tittel, C. Li, N. P. Sanchez, H. Wu, C. Zheng, Y. Yu, A. Sampaolo, and R. J. Griffin, Opt. Express **24**, A528–A535 (2016).
[6]M. Giglio, P. Patimisco, A. Sampaolo, A. Zifarelli, R. Blanchard, C. Pfluegl, M. F. Witinski, D. Vakhshoori, F. K. Tittel, and V. Spagnolo, Appl. Phys. Lett. **113**, 171101 (2018).
[7]E. Wu, D. Wu, C. Jia, Y. Wang, H. Yuan, L. Zeng, T. Xu, Z. Shi, Y. Tian, and X. Li, ACS Photonics **6**, 565–572 (2019).
[8]K. F. Mak, L. Ju, F. Wang, and T. F. Heinz, Solid State Commun. **152**, 1341–1349 (2012).
[9]C.-H. Liu, Y.-C. Chang, T. B. Norris, and Z. Zhong, Nat. Nanotechnol. **9**, 273–278 (2014).
[10]X. Chen, X. Lu, B. Deng, O. Sinai, Y. Shao, C. Li, S. Yuan, V. Tran, K. Watanabe, T. Taniguchi, D. Naveh, L. Yang, and F. Xia, Nat. Commun. **8**, 1672 (2017).
[11]F. D. P. Alves, G. Karunasiri, N. Hanson, M. Byloos, H. C. Liu, A. Bezinger, and M. Buchanan, Infrared Phys. Technol. **50**, 182–186 (2007).
[12]A. Pohlkötter, U. Willer, C. Bauer, and W. Schade, Appl. Opt. **48**, B119–B125 (2009).
[13]U. Willer, A. Pohlkütter, W. Schade, J. Xu, T. Losco, R. P. Green, A. Tredicucci, H. E. Beere, and D. A. Ritchie, Opt. Express **17**, 14069–14074 (2009).
[14]J. Ding, T. He, S. Zhou, L. Zhang, and J. Li, Appl. Phys. B **124**, 78 (2018).
[15]C. Lou, H. Chen, X. Li, X. Yang, Y. Zhang, J. Yao, C. Chang, and X. Liu, Opt. Express **29**, 20190–20204 (2021).
[16]Y. Ma, Y. He, Y. Tong, X. Yu, and F. K. Tittel, Opt. Express **26**, 32103–32110 (2018).
[17]Y. Ma, Y. He, P. Patimisco, A. Sampaolo, S. Qiao, X. Yu, F. K. Tittel, and V. Spagnolo, Appl. Phys. Lett. **116**, 011103 (2020).
[18]Q. Zhang, J. Chang, Z. Cong, and Z. Wang, IEEE Photonics Technol. Lett. **31**, 1592–1595 (2019).
[19]L. Xu, N. Liu, S. Zhou, L. Zhang, B. Yu, H. Fischer, and J. Li, Opt. Express **28**, 5648–5657 (2020).
[20]S. Dello Russo, A. Zifarelli, P. Patimisco, A. Sampaolo, T. Wei, H. Wu, L. Dong, and V. Spagnolo, Opt. Express **28**, 19074–19084 (2020).
[21]P. Patimisco, A. Sampaolo, M. Giglio, V. Mackoviak, H. Rossmadl, B. Gross, A. Cable, F. K. Tittel, and V. Spagnolo, Opt. Lett. **43**, 1854–1857 (2018).
[22]P. Patimisco, A. Sampaolo, M. Giglio, S. Dello Russo, V. Mackowiak, H. Rossmadl, A. Cable, F. K. Tittel, and V. Spagnolo, Opt. Express **27**, 1401–1415 (2019).
[23]R. Oria, J. Otero, L. González, L. Botaya, M. Carmona, and M. Puig-Vidal, Sensors **13**, 7156–7169 (2013).
[24]E. Calabrese and W. B. Fowler, Phys. Rev. B **18**, 2888–2896 (1978).
[25]M. He, W. Yan, Y. Chang, K. Liu, and X. Liu, Vib. Spectrosc. **101**, 52–63 (2019).
[26]J. Kischkat, S. Peters, B. Gruska, M. Semtsiv, M. Chashnikova, M. Klinkmüller, O. Fedosenko, S. Machulik, A. Aleksandrova, G. Monastyrskyi, Y. Flores, and W. T. Masselink, Appl. Opt. **51**, 6789–6798 (2012).
[27]A. D. Rakić, A. B. Djurišić, J. M. Elazar, and M. L. Majewski, Appl. Opt. **37**, 5271–5283 (1998).
[28]M. N. Polyanskiy, see https://refractiveindex.info for "Refractive Index Database."
[29]H. W. Lord and Y. Shulman, J. Mech. Phys. Solids **15**, 299–309 (1967).
[30]I. E. Gordon *et al.*, J. Quant. Spectrosc. Radiat. Transfer **203**, 3–69 (2017).
[31]P. Patimisco, A. Sampaolo, Y. Bidaux, A. Bismuto, M. Schott, J. Jiang, A. Muller, J. Faist, F. K. Tittel, and V. Spagnolo, Opt. Express **24**, 25943–25954 (2016).
[32]P. Patimisco, G. Scamarcio, F. K. Tittel, and V. Spagnolo, Sensors **14**, 6165–6206 (2014).
[33]H. Wu, L. Dong, H. Zheng, Y. Yu, W. Ma, L. Zhang, W. Yin, L. Xiao, S. Jia, and F. K. Tittel, Nat. Commun. **8**, 15331 (2017).